Direct Tests of Black Hole Accretion Rate Prescriptions: I. Bondi Accretion at Different Scales

James Agostino,[1] Ming-Yi Lin,[1] Natasha Jones,[1] Anne M. Medling,[1]
Loreto Barcos-Muñoz,[2,3] Daniel Anglés-Alcázar,[4] Claudio Ricci,[5,6] George C. Privon,[7,8,9]
Vivian U,[10] Paul Torrey,[11,12,13] Philip F. Hopkins,[14] and Claire Max[4]

[1]Ritter Astrophysical Research Center and Department of Physics & Astronomy, University of Toledo, Toledo, OH
43606, USA
[2]National Radio Astronomy Observatory, 520 Edgemont Road, Charlottesville, VA, 22903, USA
[3]Department of Astronomy, University of Virginia, 530 McCormick Road, Charlottesville, VA, 22903, USA
[4]PLACEHOLDER
[5]Instituto de Estudios Astrofísicos, Facultad de Ingeniería y Ciencias, Universidad Diego Portales, Avenida Ejercito
Libertador 441, Santiago, Chile
[6]Kavli Institute for Astronomy and Astrophysics, Peking University, Beijing 100871, China
[7]National Radio Astronomy Observatory, 520 Edgemont Road, Charlottesville, VA 22903
[8]Department of Astronomy, University of Florida, P.O. Box 112055, Gainesville, FL 32611, USA
[9]Department of Astronomy, University of Virginia, 530 McCormick Road, Charlottesville, VA 22904, USA
[10]4129 Frederick Reines Hall, Department of Physics and Astronomy, University of California, Irvine, CA 92697,
USA
[11]Department of Astronomy, University of Virginia, 530 McCormick Road, Charlottesville, VA 22904
[12]Virginia Institute for Theoretical Astronomy, University of Virginia, Charlottesville, VA 22904, USA
[13]The NSF-Simons AI Institute for Cosmic Origins, USA
[14]IPAC, California Institute of Technology, 1200 East California Boulevard, Pasadena, CA 91125, USA

ABSTRACT

We present spatially resolved parsec-scale measurements of nuclear conditions (gas density and kinetic temperature) relevant for black hole accretion rate predictions in the Seyfert 2 galaxy, NGC 1068. We inject these parameters into the prescription for a Bondi-like accretion model, then compare the resulting accretion rate prediction to the empirical accretion rate derived from hard X-ray observations. Cosmological simulations have spatial resolution ranging between, from $\sim$10 pc to on order kpc, and so for reasonable comparison we test these accretion rate predictions in pixel-sized radial steps out to 500 pc. Compared to warm H_2 gas, CO gas is the dominant mass carrier close to the SMBH. We find that the Bondi accretion rate ($\dot{M}_{\mathrm{Bondi}}$) of cold molecular gas alone (measured using CO) overestimates the true accretion rate by up to 4 dex in a small aperture (r$\lesssim$6 pc) around the black hole, but that it performs much better on large (r$\gtrsim$300 pc) scales. These results are the first in a series of direct tests of accretion rate prescriptions, and they suggest that using a Bondi accretion formalism to model supermassive black hole accretion in Seyfert 2 galaxies may lead to overestimated accretion rates depending on the resolution of the simulation.

1. INTRODUCTION

Supermassive black holes (SMBHs), despite their small gravitational radius of the sphere

of influence (1∼100 pc), are thought to be a key piece of the connection between pc and kpc scales of galaxy evolution. Observations of galaxies with active galactic nuclei (AGN) have shown both directly and indirectly that AGN can inject energy into their surrounding environments, which can ultimately quench or in some cases trigger star formation (see Fabian 2012 for a review).

Active galactic nuclei do not only interact with the central part of galaxies, they may also significantly impact several global properties of galaxies and their surrounding intergalactic media, allowing us to indirectly infer their influence on those observables. Relationships between black hole mass and global galaxy properties, like the velocity dispersion of stars in the galactic bulge, have been well-calibrated and show tight correlations (see Kormendy & Ho 2013; McConnell & Ma 2013 for reviews). These correlations suggest that AGN radiative feedback, which in part depends on black hole mass, may leave an imprint on bulge stellar velocity dispersion (see Ferrarese & Merritt 2000; Gebhardt et al. 2000 for seminal studies). Star formation in massive halos is suppressed (e.g. in Behroozi et al. 2013; Torrey et al. 2014), which could be caused by heating of the interstellar medium (ISM) from AGN feedback. In the high energy regime, a discrepancy is found between the observed and expected correlations between X-ray luminosities and temperatures of gas in the intra-cluster medium (called the L_X-T relation, see Mushotzky 1984; Markevitch 1998). This discrepancy suggests that gas in the intra-cluster medium evolves differently from dark matter; energetics input by host AGN could be a factor as to why.

Indirect cases of the impact of AGN feedback on galaxy formation histories are only made more intriguing by direct evidence of AGN feedback. Since more than 100 years ago (M87; Curtis 1918) radio jets powered by a central SMBH have been seen to extend up to ∼0.9 Mpc outside from their host galaxies (e.g. Centaurus A; Burns et al. 1983). Outflows driven by these SMBHs have been observed in the process of depleting the ISM at outflow rates of 700 $M_\odot$ yr^{-1} (e.g. in Mrk 231; Feruglio et al. 2010) . Our pilot galaxy for this study, NGC 1068, has a complex and well studied AGN-driven outflow that also impacts the ISM on sub-kpc scales (e.g.Wilson & Ulvestad 1983; Müller-Sánchez et al. 2011; García-Burillo et al. 2014; Saito et al. 2022; Hviding et al. 2023; Holden & Tadhunter 2023; Gallimore & Impellizzeri 2023; Mutie et al. 2024; Hagiwara et al. 2024).

The energy output of an AGN is driven by mass accretion onto its accretion disk, fueled by inflows in the nuclei of galaxies. This gas then accelerates to speeds of up to > 0.1c in the accretion disk, and that disk can power radiative outflows. The direct observational feedback can be classified as two mechanisms: radiative (quasar mode) or kinematic (radio mode) (Fabian 2012). In the quasar mode, occurring when the black hole accretes mass quickly, photons from the accretion disk couple to the ISM, transferring momentum in a powerful jet. In radio mode, accretion onto the disk is slower, and the primary feedback mechanism is in the form of collimated radio jets that typically appear narrower than quasar-mode jets (see Cielo et al. 2018 for a simulated comparison between the feedback of the two modes). Both modes can drive outflows, but the quasar-mode is thought to start the quenching process (the spatial extent of which grows over time) and then the radio-mode maintains that quenched state (see Fabian 2012 and Morganti 2017 for reviews).

As simulations of galaxy evolution have been informed by increasingly detailed observations, theorists have begun to study the physical mechanisms that drive AGN feedback and how that feedback impacts the simulated host galaxies. Dubois et al. (2013a) (see also Dubois et al.

2013b; Taylor & Kobayashi 2015) examined how AGN jets impact cold gas and transform blue, disky galaxies into red ellipticals. Building on these studies, Rosas-Guevara et al. (2015), who simulated accretion in galaxies of varied halo mass, find that in galaxies with M_{Halo} above $10^{11.5}$ $M_\odot$, as was observed in Behroozi et al. (2013), star formation is suppressed by AGN feedback. Valentini et al. (2020) perform a suite of cosmological simulations in which they couple AGN feedback to different phases of the ISM. They find, in part, that energy output from the AGN as feedback must couple with both the cold and hot phases in order to avoid excessive SMBH growth.

As is seen in both observations and simulations, global galaxy properties can be affected by accretion-dependent feedback. Theorists have attempted to model the physical processes causing those properties to change. Williamson et al. (2020) perform radiation hydrodynamics modeling of the 1-100 pc scales in a nuclear region of a simulated AGN host. They demonstrate that increasingly polar winds are produced when anisotropic radiation from the AGN shifts the mass distribution of the outflow originating from the AGN. Meenakshi et al. (2022) simulated the direct interaction between AGN jet-induced outflows on 2 kpc scale and the ISM and found shocked emission fronts in the ISM that could be responsible for stunting star formation. On r < 1 pc scale, Wada et al. (2023) were able to induce radiation-driven dusty outflows which impact the ISM as they continue on their outward paths. Tying the small and large scales together has been an ongoing challenge.

Due to computational constraints, large-scale cosmological simulations that can model hundreds of Mpc^3 at a time are not able to directly resolve the physical processes that drive gas accretion at <<1 pc scales where accretion takes place, and so sub-grid prescriptions for black hole accretion and its subsequent feedback must be adopted.[1] The 'sub-grid' is defined as the region below the gridded resolution of the simulation. Unfortunately, there is no unified model for these sub-grid physics, and different studies use different accretion prescriptions. The most commonly applied prescription is the one described in (Bondi 1952), often referred to as Bondi accretion. The equation follows the form:

$$\dot{M}_{Bondi} = \frac{4\pi G^2 M_{BH}^2 \rho}{\left(c_s^2 + v_{rel}^2\right)^{3/2}} \qquad (1)$$

where G is the gravitational constant, M_{BH} is the mass of the black hole, ρ is the gas density, c_s is the sound speed, and v_{rel}^2 is the relative velocity of the gas. In the pure Bondi case, the gas is assumed to be stationary relative to the galactic potential, so v_{rel}^2 is zero. This model accretes particles onto the supermassive black hole by initiating free fall onto the SMBH once the particle reaches the Bondi radius $R_{Bondi} = 2GM_{BH}/c_s^2$, which is typically on order 0.1-300 pc if we assume c_s of 400 km s^{-1} and SMBH mass range of $10^6 \sim 10^9$ $M_\odot$. This radius is where the escape velocity of the SMBH (based on its mass) equals the sound speed of the gas in the nuclear region. Some large scale cosmological simulation suites use a pure Bondi prescription to account for SMBH accretion, like *MassiveBlack-II* (Khandai et al. 2015), *EAGLE* (Schaye et al. 2015), and *IllustrisTNG* (Weinberger et al. 2017; Pillepich et al. 2018a).

Physically, the issue with the Bondi accretion formalism is that it ignores both the angular momentum of the gas and interactions due to self-gravity between gas particles, which is only appropriate in the case of hot, virialized gas (Hobbs et al. 2012). Recent studies have shown that gas and other accreting material still

---

[1] Although there is also much variation in AGN feedback prescriptions, this program will focus on discussing the accretion rate prescriptions, on which all feedback depends.

has angular momentum inside what may be the Bondi radius, particularly in gas-rich mergers or galaxies with Seyfert AGN (e.g. in Davies et al. 2004; Hicks et al. 2013; Medling et al. 2014; Lin et al. 2016), and so Bondi accretion timescales may be much shorter than in reality where angular momentum delays accretion.

To account for this problem, some large-scale cosmological simulation suites apply accretion physics by using modified versions of Bondi accretion. The prescription in the *Illustris* (the predecessor to *IllustrisTNG*; Vogelsberger et al. 2013; Genel et al. 2014) and *Magneticum Pathfinder* hydrodynamical simulation suites (Hirschmann et al. 2014; Bocquet et al. 2016; Dolag et al. 2016) modify Bondi by multiplying Equation 1 by a constant (unitless) 'boost' factor α (following the prescription of Springel et al. 2005; Di Matteo et al. 2005; Springel & Hernquist 2005). The boost factor is used to account for the volume average of the Bondi-rates for both the cold and hot phases in the simulations and typically has a value = 100. Another large-scale cosmological model, *Horizon-AGN* (Dubois et al. 2016), uses an α similar to *Illustris* and *Magneticum*, but instead of a constant value, their boost factor (following the prescription from Booth & Schaye 2009) depends on density of the gas. Another approach, used by the large-scale *Romulus* suite (Tremmel et al. 2017) is to adjust the Bondi accretion rate depending on the motion of the simulated gas particles. In *Romulus*, if the smallest relative velocity (which they equate to v_{bulk}, the bulk motion of the gas) of the gas particle closest to the SMBH is faster than the rotational velocity of the gas, they replace the relative velocity of the SMBH with v_{bulk} and multiply the Bondi rate by a boost factor dependent on gas density.

Bondi or Bondi-like accretion prescriptions are the most commonly used, but theorists have also designed accretion prescriptions with very different underlying physics. One large-scale simulation ($[100 \ h^{-1} \ \mathrm{Mpc}]^3$ volume) suite that in part uses one of these prescriptions is *SIMBA* (Davé et al. 2019a). In *SIMBA*, pure Bondi accretion is still applied for hot gas accretion where, as we mentioned, it is most appropriate. But, they then apply a torque-limited accretion formalism for the cold gas where instabilities in the disk drive mass inflow (Hopkins & Quataert 2011; Anglés-Alcázar et al. 2017). Understanding if and in which cases different sub-grid prescriptions are accurately estimating accretion rates onto the black holes of galaxies is critically important to cosmological simulations. *Without an accurate prescription for accretion over time, simulations cannot accurately implement the impact of AGN feedback, and as such may have incorrect outcomes with regards to galaxy formation and evolution.*

Observationally testing how black hole accretion rate prescriptions perform has only become possible in recent times. In this study, we directly measure the parameters that go into Bondi accretion, ρ_{gas} and c_s, on physical scales ranging from 2-170 pc. We then plug these measured parameters into the pure Bondi accretion prescription as a function of radius to mimic what a simulation at that resolution would estimate for the black hole accretion rate. Finally we test these predicted Bondi accretion rates against empirically derived accretion rates using hard (14-195 keV) X-ray data from the The Burst Alert Telescope (BAT) AGN Spectroscopic Survey (BASS) survey (Ricci et al. 2017). The BAT instrument (Barthelmy et al. 2005; Krimm et al. 2013) on *Swift* (Gehrels et al. 2004) is a hard X-ray detector that surveys the entire sky, reporting X-ray sources to within 1-4 arcmin accuracy.

In this work, we use cosmological parameters of $H_0 = 70$ km s^{-1} Mpc^{-1}, $\Omega_m = 0.28$, and $\Omega_\Lambda = 0.72$ (Hinshaw et al. 2009). To calculate spatial scales and luminosity distance to NGC
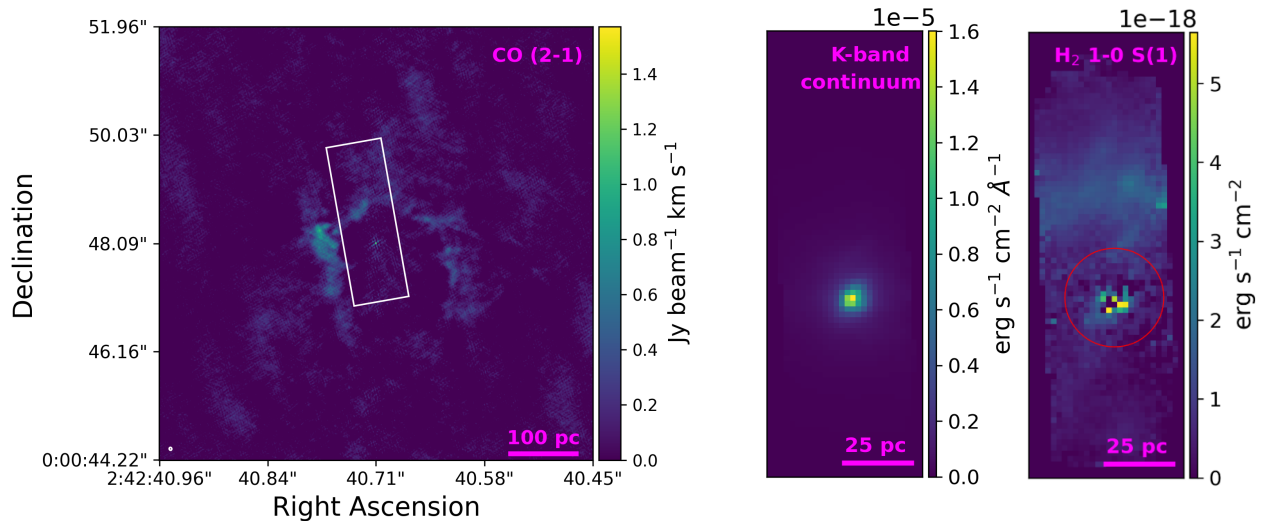
Figure 1. Nuclear region of NGC 1068 in the CO(2-1) flux (left, from ALMA), 2.2μm continuum (middle), and the continuum subtracted rovibrational H_2 1-0 S(1) transition (right), described in Section 2. The CO(2-1) moment 0 map is masked below 3×rms and the white box in the CO(2-1) moment map represents the field of view of the NIR data. The very small, white ellipse in the bottom left represents the beam size of the ALMA data (41×30 mas). All three images show flux peaks at the AGN's location and both the CO and H_2 maps have enhanced emission in the CND ring. The red circle in the H_2 1-0 S(1) moment map represents the aperture in which T_{Kin} is calculated in Figure 3.

1068 we use Ned Wright's Cosmology Calculator (Wright 2006).

2. NGC 1068 OBSERVATIONS

For NGC 1068, we made use of <3 pc scale resolution both in the near infrared (NIR) with Keck/OSIRIS+AO (adaptive optics; PI Medling), and in the sub-mm with ALMA archival data (PI García-Burillo).

2.1. *Keck/OSIRIS K-band Integral Field Spectroscopy*

The first of two sets of data we are using in this project is a set of high resolution integral field unit (IFU) Keck/OSIRIS+AO (OH-Suppressing InfraRed Imaging Spectrograph, Larkin et al. 2006) integrations, for which we mosaic all frames into a single data cube. These observations were taken with the Kbb filter (broad-band K between 1.965 - 2.381 μm) with the 35 mas pixel^{-1} plate scale on 2018 December 28th, 2019 January 22nd, and 2019 October 7th for a total exposure time of 6120 seconds

(51 frames, 120 seconds each). Weather impacted observations on 2019 October 7th, during which the laser guiding system was also not working. We used the galaxy nucleus as the natural guide star in NGS mode, and as the tip/tilt star in LGS mode. AO corrections in those frames without the laser produced larger point spread functions with full-width at half-maximum (FWHM) values between 3 and 5 pixels compared to ~2 with the laser on other nights. We reduced the Keck/OSIRIS+AO observations using the OSIRIS Data Reduction Pipeline (OSIRISDRP, Lyke et al. 2017; Lockhart et al. 2019) version 4.2.0, which we use to extract a spectrum for each spatial pixel, assemble the spectra into a cube, and mosaic the 51 total frames together to form the final image, which has a 0.17" point spread function (PSF) FWHM. Flux calibration was applied for each night before final mosaicking.

The resulting mosaic reveals a strong K-Band continuum (particularly near the AGN) and

H$_2$ 1-0 rovibrational emission (S(0), $\lambda_{\rm rest} =$ 2.2235μm; S(1), $\lambda_{\rm rest} = 2.1218\mu$m; S(2)), $\lambda_{\rm rest} =$ 2.0338μm. These continuum and continuum-subtracted H$_2$ 1-0 S(1) maps are shown in the middle and right panels of Figure 1 respectively. The continuum map was made using the Cube Analysis and Rendering Tool for Astronomy (CARTA, Comrie et al. 2021) and the continuum subtracted H$_2$ 1-0 S(1) map was made using QFitsView (Ott 2012). Both images show peaks of emission on or near the position of the central engine, and NGC 1068's circumnuclear disk (CND) ring can be seen in the H$_2$ map.

2.2. ALMA Band 6 Long-baseline Interferometry

We chose the highest resolution CO J =(2-1) (hereafter CO(2-1)) available on the ALMA archive that shows strong emission (PI García-Burillo, Project code 2016.1.00232.S; see also García-Burillo et al. 2019). We retrieved the CO(2-1) spectral cube product from the ALMA archive, which has a rms of 0.25 mJy over 20 km s^{-1}, and was imaged using a Briggs (Briggs 1995) robust value of 0, resulting in a beam size of 41 × 30 mas. We then used this spectral cube with the image cube analysis tools in CARTA (Comrie et al. 2021) to create a moment 0 (flux) map of the CO(2-1) emission. Figure 1 (left) shows this CO(2-1) moment 0 map which is masked below 3×rms and is used for our analysis in Section 3. Like in the warm H$_2$ observations, both the AGN and CND ring are bright sources in CO(2-1).

2.3. Nuclear structure of NGC 1068

NGC 1068 is one of the most-studied prototypical Seyfert galaxies, and as such a wealth of information has already been published about its nuclear structure. The studies described here are not an exhaustive list, but are included to provide context relevant to our analysis.

Under our 2.2 pc resolution, NGC 1068 hosts a water maser that is thought to originate from the accretion disk on much smaller (<0.1 pc) scales. Greenhill et al. (1996) observed the maser with very long baseline interferometry (VLBI) using both the Very Long Baseline Array and Very Large Array to achieve 0.65 pc resolution. They used the velocity gradient of the maser emission to infer a rotational velocity of the gas, and in turn constrain M$_{\rm BH}$. Kumar (1999) modeled the 0.65-1.1 pc disk from which the maser emission is thought to be ejected from. The clumps in their disk model interact with each other, leading to eventual accretion onto the SMBH.

On slightly larger scales with near and mid infrared interferometry, multiple authors were able to resolve a two-component dusty torus (Jaffe et al. 2004; Raban et al. 2009). One component is smaller and more elongated (1.35 × 0.45 pc) in size than the other (3 × 4 pc). In the nucleus of Circinus, another Seyfert 2 AGN, Tristram et al. (2014) also found a two-component dusty torus. Images like these that showed structure inconsistent with the prior, observationally-defined, Type 2 classification of these galaxies (unless foreground extinction was applied) fundamentally challenged the AGN unification model (Antonucci 1993).

Gámez Rosas et al. (2022) used sub-pc resolution observations of NGC 1068 taken with the MATISSE/ESO/VLTI interferometer between 3 and 13 μm to map the dust temperature distribution of the dust observed in the previously mentioned studies. They confirm an optically thick pc scale dusty structure and a second, less optically thick disk that extends to at least 10 pc. García-Burillo et al. (2019) (who in part use the same ALMA data as we describe in Section 2.2) find a 14 pc CO(2-1) nuclear disk with a PA (~110-140 deg) aligned with the water maser disk PA (140 deg). Also in García-Burillo et al. (2019), they observe the CND, which as can be seen in Figure 1, has a gas deficit inside the outer ring in its central ~ 130 pc region.

To resolve the kinematics of the 10 pc inner disk (often referred to as the torus) and outer ring, Imanishi et al. (2020) observe both of these scales using the bright (relative to CO(2-1)) HCN J=(3-2) and HCO+ J = (3-2) transitions with ALMA at 1.4 pc resolution. They find that the torus as observed with these dense gas tracers rotates in the opposite direction with respect to the outer ring. This is particularly surprising because the water maser emission is rotating in the same direction as the outer ring rather than the torus it is physically closer to (see Figure 1 of Imanishi et al. 2020). In the work of García-Burillo et al. (2019), the authors find that a "significant part" of the observed counter-rotation in CO(2-1) can be attributed to a northern AGN-driven wind. To make a more robust determination though, García-Burillo et al. (2019) say that higher resolution data is required so that the outflowing component can be better disentangled from the rotating component.

Outflows originating from the AGN can serve to regulate black hole accretion, and NGC 1068 hosts a complex outflow in the NE direction, perpendicular to the nuclear disk. The largest outflow component is seen as the radio jet (e.g. in Gallimore et al. 1996). Mutie et al. (2024) present higher resolution (∼4 pc) e-MERLIN 5 GHz data along with archival VLA 10 GHz, and VLA 21 GHz images of the jet. These images together show not only the central jet emission, but also detail in the larger scale bow shock, >200 pc from the SMBH in the same NE direction, which exhibits direct evidence of the AGN's impact on the ISM. The impact of the jet on the ISM is studied in part in both Hviding et al. (2023) and Holden & Tadhunter (2023), who both show evidence for gas ionization consistent with shock ionization or radiation-bounded AGN-photoionization along the outflow's path on 160 pc to kpc scale. García-Burillo et al. (2014) show that the CO kinematics on distances 50 to 400 pc are spatially correlated with the radio jet, evidence that the AGN is influencing even the cold ISM. ALMA CO(6-5) observations from Gallimore et al. (2016) show that this molecular outflow originates within 2 pc from the SMBH, and has velocities relative to systemic of about 400 km s^{-1}. This outflow may have an impact on our measurements of molecular gas mass, but that impact is expected to be small as there is not much CO(2-1) emission between the AGN and CND ring, and the CND ring itself does not appear very disturbed along the path of the outflow.

3. PRESCRIPTION PARAMETERS

In this pilot study, we examine the performance of the most commonly used accretion prescription for black hole growth in NGC 1068. The Bondi accretion formalism with a relative velocity of zero (also known as Bondi-Hoyle, or Bondi-Hoyle-Lyttleton e.g. Hoyle & Lyttleton 1939; Bondi & Hoyle 1944; Bondi 1952) follows the form:

$$\dot{M}_{Bondi} = 4\pi G^2 M_{BH}^2 \rho c_s^{-3} \qquad (2)$$

where G is the gravitational constant, M_{BH} is the mass of the black hole, ρ is the gas density and c_s is the sound speed.

Bondi accretion is predicated on a spherically symmetric, non-self-gravitating gas distribution in which the gas inside the Bondi radius has no angular momentum. While this kind of environment may not be most appropriate for describing all galaxy nuclei (see Section 5 for additional information), Bondi accretion is a simple analytical prescription that can be applied inside a sphere of any radius, which makes it convenient as a sub-grid prescription.

In this subsection, we outline the methods for measuring each free parameter in the Bondi prescription using the available high resolution data from Section 2.

3.1. *Parameter 1: black hole mass*

Greenhill et al. (1996) imaged NGC 1068's water maser emission at a 0.65 pc scale using very long baseline interferometry. From the rotation curve of the water maser emission, they found the enclosed mass within that radius to be $\sim 1 \times 10^7$ M$_\odot$(with uncertainty on order unity). Another study by Lodato & Bertin (2003) derive a smaller black hole mass of $\sim 8 \pm 0.3 \times 10^6$ in a self-gravitating accretion disk model that matches the Greenhill et al. (1996) and Greenhill & Gwinn (1997) observations well. The Lodato & Bertin (2003) model corrects for non-Keplerian motion in the velocity profile of the water maser emission, but this could be an over-correction. In fact, other studies have found that the disk rotation may still be dominated by the black hole (Imanishi et al. 2018). Albeit with a worse fit to the velocities from the maser emission, Lodato & Bertin (2003) also fit a Keplerian rotation model, which has a best fit black hole mass of $\sim 1.5 \pm 0.02 \times 10^7$ M$_\odot$. In the absence of clear evidence in favor of one of the newer modeling schemes, we adopt the Greenhill et al. (1996) value of M$_{\rm BH} = \sim 1 \times 10^7$ M$_\odot$ as an intermediate M$_{\rm BH}$ measurement.

3.2. *Parameter 2: gas density*

3.2.1. *Choice of volume element*

To measure the gas density, we first must define our volume element. In cosmological simulations, typically, a fixed number gas particles exist inside a spherical region with radius r centered on the location of the SMBH. This volume makes up the black hole kernel, in which the accretion physics are prescribed. Although studies like the ones discussed in Section 2.3 and Vollmer et al. (2022) have shown that ~ 10 pc cold gas distribution is more disk-like, we opt to use a sphere of volume V $= \frac{4}{3}\pi r^3$ centered on the AGN for which we vary the radius with the goal of mimicking the accretion resolution elements found in simulations that use Bondi accretion.

3.2.2. *Cold gas mass*

To measure the molecular gas (H$_2$ and He) mass inside the sphere, we use the CO(2-1) data described in Section 2.2. To obtain a molecular gas mass, we utilize the conversion factor $\alpha_{\rm CO}$. The exact value of $\alpha_{\rm CO}$ depends on several factors including the size scale and environment over which the CO flux is measured. The picture is further complicated by the distinction between $\alpha_{\rm CO(1-0)}$ and $\alpha_{\rm CO(2-1)}$, where the difference is dictated by the ratio between the line luminosity of the two rotational transitions: r$_{21}$ (r$_{21} = {\rm L}'_{\rm CO(2-1)}/{\rm L}'_{\rm CO(1-0)}$), which depends on the temperature of the gas. In this work, we follow the same $\alpha_{\rm CO}$ methodology as in García-Burillo et al. (2019) who use the Milky Way $\alpha_{\rm CO(1-0)} = 4.3 \pm 1.29$ M$_\odot$(K km s^{-1}pc^2)$^{-1}$ recommended by Bolatto et al. (2013). We use $\alpha_{\rm CO(1-0)}$ in conjunction with the the averaged line intensity ratios for NGC 1068's northern and southern CND regions (because the CND ring contains the majority of the nuclear gas mass): r$_{21} = 2.2 \pm 0.4$, from Viti et al. (2014) to calculate a final

$$\alpha_{\rm CO(2-1)} = \frac{\alpha_{\rm CO(1-0)}}{{\rm r}_{21}} = \frac{4.3 \pm 1.29}{2.2 \pm 0.4}$$
$$= 1.95 \pm 0.73 \ M_\odot({\rm K \ km \ s}^{-1} \ {\rm pc}^2)^{-1}. \quad (3)$$

The outflowing components of NGC 1068 may have a lower $\alpha_{\rm CO(1-0)}$, but we expect the Milky Way value to be closer to the average for the purpose of measuring integrated enclosed masses, especially at larger r. $\alpha_{\rm CO(2-1)}$ is then multiplied by the sum of the flux density inside a circular aperture of radius r, to match our spherical geometry. The enclosed mass profile is shown alongside a snapshot of the aperture geometry in Figure 2. García-Burillo et al. (2019), who center their r = 200 pc aperture measurement on the center of the CND ring, find a molecular (H$_2$ + helium) gas mass of $\approx 1.4 \times 10^8$ M$_\odot$. We measure molecular gas mass within the same aperture (using CARTA to measure flux) and find $1.3 \pm 0.5 \times 10^8$ M$_\odot$ (1.4
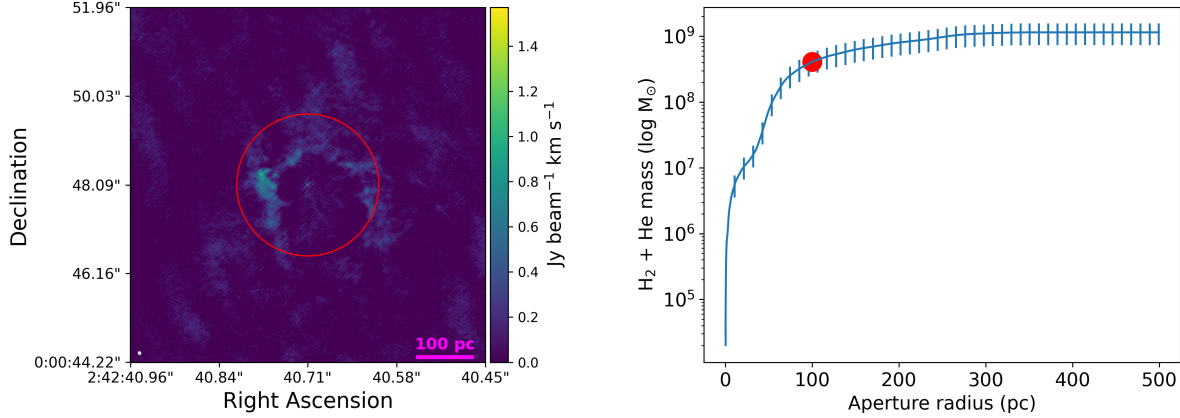
Figure 2. *Left*: Moment 0 map of CO(2-1) in NGC 1068, with flux density values masked below 3×rms. The red circle indicates the location and size of the 100 pc aperture (centered on the AGN) corresponding to the red dot in the right panel, which has $M_{enc,H_2+He} = 4.09 \pm 1.49\times10^8$ M$_\odot$. The small, white ellipse in the bottom left represents the beam size of the ALMA data (41×30 mas). *Right*: Integrated mass profile inside the radial aperture. Details on the conversion to molecular gas mass can be found in Section 3.2.

$\pm\ 0.5\ \times\ 10^8$M$_\odot$ if centered on the AGN), both of which are consistent with the García-Burillo et al. (2019) measurement. For comparison to another nearby Seyfert 2, in the nuclear region of Circinus, using the warm H$_2$ gas tracer H2 1-0 S(1), Müller Sánchez et al. (2006) find the total molecular gas mass to be 1.7×10^7 M$_\odot$ within 0.8" (52pc). Integrated inside the same physical distance from the SMBH in NGC 1068, we find a molecular gas mass of $8.8 \pm 3.2\times 10^7$ M$_\odot$, higher by almost 1 dex.

To convert enclosed mass to density we divide by the volume element for a sphere (see Section 3.2.1) with r defined by our circular aperture size used for measuring mass. In this sphere with r = 100 pc centered on the AGN as shown in Figure 2 (left), we find a molecular gas mass density of 93.3 ± 71.1 M$_\odot$pc^{-3}.

3.2.3. *Warm H$_2$ gas mass*

We also calculate an enclosed mass using the warm H$_2$ gas measured from the NIR data, following Equation 6 of Storchi-Bergmann et al. (2009), which uses the line flux of the H$_2$ 1-0 S(1) rovibrational transition at $\lambda_{rest} = 2.1218$ μm. In NGC 1068, Martins et al. (2010) used the NASA 3-m Infrared Telescope Facil-

ity (IRTF) and found a nuclear (slit 1"x 2") extinction E(B-V) of 1.13 (from their Table 4). Assuming the standard extinction law of Cardelli et al. (1989) with R$_v$ = 3.1, the extinction A$_v$ (A$_v$ = R$_v$ × E(B-V)) is ∼3.5. Based on A$_k$∼A$_v$/10 (Howarth 1983), the extinction-corrected H$_2$ gas mass inside r <1.7" (111 pc) is ∼68 M$_\odot$, which is about 1.38 times the observed value. The warm H$_2$ mass is inconsequential compared to the CO-derived value of $4.08 \pm 1.49\times10^8$ M$_\odot$ in the same region.

One reason that the warm gas measurement in this subsection may be so small is due to the radiative environment in NGC 1068's nucleus. Under local thermal equilibrium (LTE, where the energy distribution can be described by a single number locally) conditions, the H$_2$ emission can be excited by the equilibrium value for temperatures T $\approx$ 1000 K (Davies et al. 2005). To reach such high excitation temperatures in NGC 1068, H$_2$ emission lines can be excited through several mechanisms, as described below:

(1) *UV fluorescence*: This excitation mechanism dominates in photodissociation regions (PDRs). Far-ultraviolet (FUV, $\lambda > 912$ Å) radiation pumps the molecule into electronically ex-

cited states, leading to subsequent cascades that emit fluorescent emission (Wakelam et al. 2017). This mechanism is dominant in Seyfert 1 galaxies (Davies et al. 2005). Although NGC 1068 is classified as a Seyfert 2 galaxy and is expected to have less FUV radiation, the HST/FOC UV image shows a bright nucleus with polarization (Barnouin et al. 2023) within our OSIRIS field of view (FOV).

(2) *Shocks and outflows*: Veilleux et al. (1997) suggest that shocks associated with nuclear outflows are a likely heating source for H_2 in many Seyfert 2 galaxies. May & Steiner (2017) analyzed VLT/SINFONI and Gemini/NIFS data with a larger FOV covering the entire CND and proposed that the CND could be an expanding bubble.

(3) *X-ray heating from the AGN*: X-ray emission can penetrate deeply into regions that are opaque to UV photons and influence H_2 excitation (Matt et al. 1997). All of these mechanisms can contribute to H_2 emission.

We measure the H_2 1-0 S(1) extinction-corrected intrinsic flux ($F_{intrinsic} = F_{observed} \times 10^{(0.4A_k)}$) and directly convert it to the warm H_2 gas mass. Due to the rectangular FOV, only an aperture radius of <0.3" is fully contained within the OSIRIS FOV, suggesting that H_2 emission at radii >0.3" is incomplete.

3.3. *Parameter 3: sound speed of the gas*

The final parameter required in the Bondi accretion formalism is the sound speed of the gas. The sound speed for an ideal gas is:

$$c_s = \sqrt{\frac{\gamma R T_K}{M}} \quad (4)$$

where γ is the adiabatic index (1, as the gas is assumed to be isothermal in each sub-region), R is the gas constant 8.3144598 J mol^{-1} K^{-1}, T_K is the temperature of the gas (K), and M is the molar mass (kg) of the gas, for which we assume solar metallicity. All but the temperature in this case are constants.

For the temperature of the molecular gas, we use two methods: one using CO rotation diagrams (cold gas), and another using an excitation diagram for the molecular H_2 (warm gas) from our Keck/OSIRIS+AO NIR data.

3.3.1. *CO-derived c_s*

For a temperature from CO transitions we refer to the work of Viti et al. (2014) who infer the temperature of the gas in the CND of NGC 1068 by using CO rotation diagrams. This method assumes that the gas is in LTE, and that the observations are mostly in the Rayleigh-Jeans regime where the intensity of the radiation is proportional to the temperature. This temperature is also known as the 'rotational temperature' and is equal to the kinetic temperature if all CO levels are thermalized (Goldsmith & Langer 1999). Because of these assumptions, this temperature should be considered a lower limit, which translates to an upper limit on our final accretion rate because $\dot{M}_{Bondi} \propto c_s^{-3}$. For the central region of NGC 1068, Viti et al. (2014) find a temperature of 50 ± 5-7 K via the CO rotation diagram method (see Section 3.1.1. of their work for more details). Plugging that and the other constants into Equation 4, we find that the speed of sound in the cold molecular gas phase is 409.2 ± 141.7 km s^{-1}.

3.3.2. *H_2-derived c_s*

As shown in Section 3.2.3, warm H_2 is also present in NGC 1068's nuclear regions, so we also consider the sound speed for this component of the ISM. To measure the temperature which we then use in the c_s calculation, we use the H_2 1-0 S(0), S(1), and S(2) rovibrational line fluxes in the Keck/OSIRIS NIR data described in Section 2.1. Assuming the H_2 gas is in LTE, the H_2 excitation temperature is equal to the kinetic temperature. Figure 3(a) shows the H_2 excitation diagram, which is the column density in the upper level of each transition normalized by its statistical weight (N_u/g_u) as a function of

energy of the level as a temperature (E_u). The best-fit slope of this relationship is related to T_K as $\frac{N_u}{g_u} \propto e^{(-\frac{h\nu}{kT_K})}$ in the LTE description of energy level populations (see pages 322, 327 of Wilson et al. 2013). Solving for T_K then yields $-\frac{1}{T_K} \propto \frac{ln\frac{N_u}{g_u}}{\frac{E_u}{k}}$.

Because we have spatially resolved data for these H_2 lines, we can derive kinetic temperatures from 12-111 pc and apply them at the matched distances in the accretion rate prediction. While the Keck/OSIRIS+AO data has a higher resolution than 6 pc, the H_2 1-0 S(1) and S(2) lines are not detected in a r≤6 pc (0.1") aperture. Fluxes of the lines are measured using the line fitting tool in `QFitsView` (Ott 2012), which we use to fit the continuum and one Gaussian component to the integrated (within a region circular region with radius r) spectrum. Figure 3(b) shows the range of excitation temperatures as a function of radius. T_K ranges from 678-2261 K, and peaks at r≤85 pc where $T_K = 2261^{+3683}_{-1631}$ K. High temperatures may be caused by the influence of the PDR (Section 3.2.2 describes observations of this for NGC 1068), which is found to increase the H_2 1-0 S(1) emission by up to 70% in the some luminous infrared galaxies (Davies et al. 2000; Davies et al. 2003). Using Equation 4 (with a molar mass of H_2) results in H_2 sound speeds between 1013-1850 km s^{-1}, peaking at r = 85 pc.

4. RESULTS: $\dot{M}_{Bondi}$ VS. $\dot{M}_{X-RAY}$

4.1. Calculating $\dot{M}_{Bondi}$

Now that we have calculated each parameter for the Bondi accretion prescription in Section 3, we are ready to estimate a Bondi accretion rate. Because our parameters are spatially resolved, we calculate accretion rate as a function of simulated resolution:

$$\dot{M}_{Bondi}(r) = 4\pi G^2 M_{BH}^2 \rho(\leq r) c_s(\leq r)^{-3}. \quad (5)$$

Figure 4 shows the Bondi accretion rate for the cold derived case as a function of radius, the means of which range between about 10^2 and 10^{-3} M$_\odot$ yr^{-1}. As the enclosed mass found in Section 3.2 for the warm H_2 gas component in r< 170 pc is small (68 M$_\odot$), and the temperature gradient is high (678-2261 K, see Section 3.3.2) relative to the values found for the cold CO gas component, the resulting Bondi accretion rates are much smaller (between about 10^{-10} and 10^{-7} M$_\odot$ yr^{-1}) for the warm gas. These results suggest that the cold gas is the dominant carrier of mass accretion on r< 170 pc scales. Table 1 shows a range of precise values for both the cold and hot Bondi accretion rates.

### 4.2. Calculating X-ray accretion rates

To understand how well the Bondi accretion formalism compares to the real accretion rate, we compare it to the X-ray derived accretion rate. To calculate an accretion rate from X-ray measurements, we use *Swift*/BAT data from the BAT AGN Spectroscopic Survey (BASS, Ricci et al. 2017). They present intrinsic luminosities in the 14-195 keV band, which we use alongside the bolometric correction, Equation 17 in Gupta et al. (2024):

$$\log(\kappa_{14-195}) = (0.13 \pm 0.04) \times \log(\lambda_{Edd})$$
$$+ (1.04 \pm 0.05) \quad (6)$$

to calculate bolometric luminosity. Because Ricci et al. (2017) measure a neutral column density of $\log N_H = 25.0$ cm^{-2} in NGC 1068 and the X-ray continuum might not be well estimated when the emission is dominated by reprocessed radiation in environments like this, we conservatively estimate uncertainty on the input intrinsic 14-195 keV luminosity to be ± 0.4 dex. We then use that bolometric luminosity in the equation from Netzer & Trakhtenbrot (2014), $L_{bol} = \eta \dot{M} c^2$, solving for $\dot{M}$ η is the unitless mass-to-radiation conversion efficiency that depends on the spin of the black hole. For stationary, retrograde disk, and maximally rotating SMBHs respectively, the values for η are
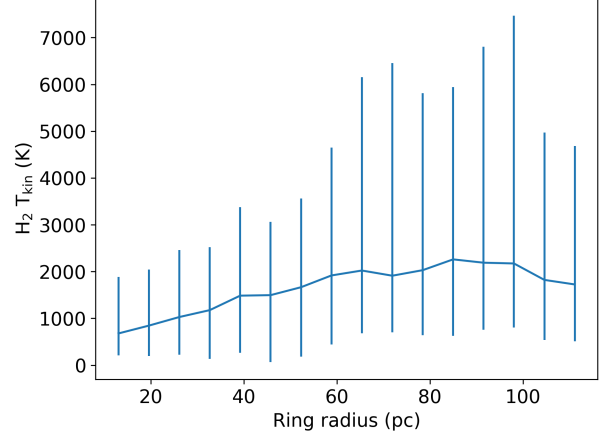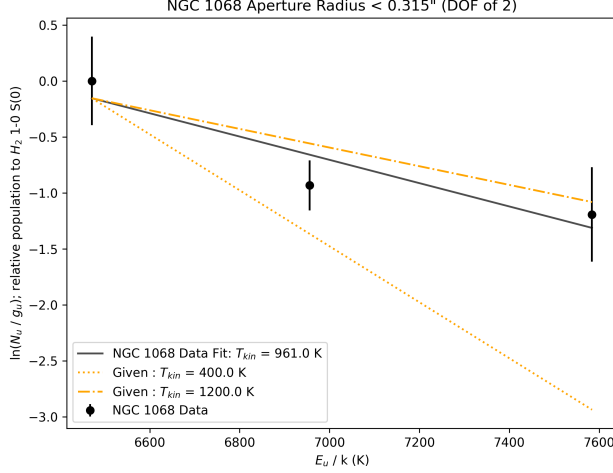
Figure 3. (*Left*:) Column density in the upper level of each H_2 1-0 S(0), S(1), and S(2) transition as a function of energy level of that transition as a temperature (K) inside a r = 21 pc circular aperture centered on the AGN as shown in Figure 1. The best fit slope (using linear regression), as described in Section 3.3.2, is the temperature of the gas in that region if we assume LTE. (*Right*:) T_K estimated as in the excitation diagram on the left but instead inside circular apertures matching the methods of Section 3.2 from 0.2" to 1.7" in steps of 0.1". The mean of the derived temperatures is 1612^{+2840}_{-1216} K.
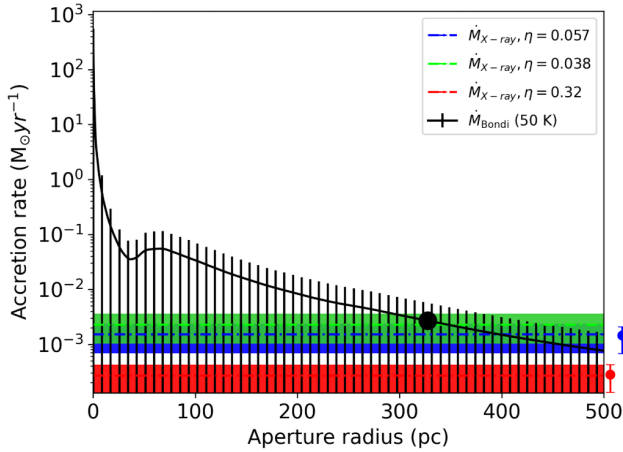
Figure 4. X-ray and (Cold-derived) Bondi accretion rates as a function of radius over which nuclear parameters are measured. Color bars and ranges displayed to the right denote uncertainties on each X-ray measurement. The Bondi prescription overestimates $\dot{M}_{BH}$ by orders of magnitude for low aperture radii, but, above 327 pc (the black circle), the mean Bondi prescription value begins to agree and even dip below the mean minimum prediction from the X-ray by aperture size r = 398 pc.

0.057, 0.038, and 0.32 (Netzer & Trakhtenbrot 2014). For NGC 1068, we find $\dot{M}_{X-ray}$ values equal to $1.51 \pm 0.81 \times 10^{-3}$ $M_\odot yr^{-1}$ (stationary SMBH), $2.26 \pm 1.21 \times 10^{-3}$ $M_\odot yr^{-1}$ (retrograde accretion disk), and $2.69 \pm 1.43 \times 10^{-3}$ $M_\odot yr^{-1}$ (maximally spinning SMBH). Figure 4 and shown in Table 1. $\dot{M}_{Bondi}$ overestimates the accretion rate by several orders of magnitude at small distances from the SMBH where the gas density is high, but dips below the X-ray accretion rates at large distances, where density is low.

Vollmer et al. (2022) used the IR-derived bolometric luminosity for the AGN in NGC 1068 from Vollmer et al. (2018) to calculate $\dot{M}_{BH} \sim L_{bol}/(0.1c^2) \sim 0.05$ $M_\odot yr^{-1}$. They calculate a mass accretion rate onto their modeled accretion disk for NGC 1068 to be 2×10^{-3} $M_\odot yr^{-1}$ ($\eta = 0.1$), which is in agreement with our $\dot{M}_{X-ray}$ values and the cold gas derived $\dot{M}_{Bondi}$ in aperture sizes of r≥363 pc.

5. DISCUSSION: RESULTS IN CONTEXT OF SIMULATIONS

To inform theorists on which accretion prescriptions in their simulations are best to use

Method	Accretion rate	(M$_\odot$ yr^{-1})				
X-rays (ϵ= 0.57)		1.51 ± 0.81	× 10^{-3}			
X-rays (ϵ= 0.38)		2.26 ± 1.21	× 10^{-3}			
X-rays (ϵ= 0.32)		2.69 ± 1.43	× 10^{-3}			
Bondi (<r)	5 pc	10 pc	25 pc	50 pc	100 pc	200 pc	500 pc
(T$_{Kin}$ = 50 K)	1.62 ± 1.79	0.43 ± 0.47	0.06 ± 0.07	0.05 ± 0.05	0.03 ± 0.04	8.32 ± 9.16×10^{-4}	7.63 ± 8.41×10^{-4}
(T$_{Kin}$ = 678-2261 K)	*	*	8.16 $^{+28.89}_{-21.6}$ × 10^{-9}	4.95 $^{+15.87}_{-14.03}$ × 10^{-10}	5.04 $^{+23.61}_{-11.20}$ × 10^{-11}	*	*

Table 1. Accretion rate measurements and estimates for rates derived from X-ray luminosities and the pure Bondi accretion prescription inside various radii. In NGC 1068, where the cold gas phase makes up the bulk of the gas mass in the nucleus, the cold gas derived Bondi accretion estimate outpaces the X-ray derived accretion rates by between 2 and 4 orders of magnitude. *H$_2$ 1-0 S(1) and S(2) lines required to calculate temperature for the Bondi calculation are not detected in this aperture.

828 and when, we have designed our measurements
829 to fit in the practical context of those simu-
830 lations. Large scale cosmological simulations
831 must use sub-grid physics for accretion because
832 of computing constraints. Some examples of hy-
833 drodynamical galaxy evolution simulations that
834 use or have popular options to use a spheri-
835 cally symmetric, Bondi or Bondi-like black hole
836 accretion formalisms are *Illustris/IllustrisTNG*
837 (Genel et al. 2014; Vogelsberger et al. 2014;
838 Pillepich et al. 2018b), *Magneticum Pathfinder*
839 (Hirschmann et al. 2014; Bocquet et al. 2016;
840 Dolag et al. 2016), *MassiveBlack-II* (Khandai
841 et al. 2015), *Eagle* (Schaye et al. 2015), *Horizon-
842 AGN* (Dubois et al. 2016), *Romulus* (Tremmel
843 et al. 2017), and *SIMBA* (Davé et al. 2019b,
844 uses Bondi for hot gas only). The resolution of
845 the hydrodynamical gas cells in which these sub-
846 grid physics are calculated ranges from to 10s of
847 pc to more typically kpc. Even in the highest
848 resolution zoom-in simulations, the spherical ra-
849 dius in which particle calculations are made is
850 approximately 10 pc (Wetzel et al. 2023).
851 Because we have spatially-resolved measure-
852 ments, we are able to examine the performance
853 of Bondi accretion at a range of spatial scales.
854 For the Bondi accretion rate derived from warm
855 gas we are limited by the field of view of OSIRIS

856 (0.56×2.24" with our observational setup), but
857 the ALMA data extends to over 500 pc away
858 from the SMBH.
859 Table 1 shows the Bondi accretion rates at
860 radii between 5-500 pc as calculated in Sec-
861 tion 4, and the X-ray accretion rates as calcu-
862 lated in Section 4.2, which are all plotted to-
863 gether in Figure 4. At aperture radii r≤327 pc,
864 the parameterized Bondi accretion rate exceeds
865 the X-ray derived accretion rate (by 2 or more
866 dex in aperture sizes of r≲15 pc and by 1 or
867 more dex when r≲125 pc).
868 This is, perhaps, not a surprising result. Past
869 studies have hinted towards Bondi accretion
870 overestimating the real accretion rate. Di Mat-
871 teo et al. (2000) found that luminosities calcu-
872 lated using estimated Bondi accretion rates for
873 six black holes with masses of 0.22-5.2 × 10^9
874 M$_\odot$ determined in Magorrian et al. (1998) were
875 4-6 orders of magnitude higher than the real lu-
876 minosities of the galaxy nuclei. Hopkins et al.
877 (2016) model SMBH accretion in a gas-rich nu-
878 clear disk in a massive simulated galaxy with 0.1
879 pc resolution. In their study, applying a pure
880 Bondi accretion formalism resulted in an accre-
881 tion rate ∼10^8 times higher than the luminosity-
882 derived accretion rate native to their simulation.
883 Near the SMBH, pure Bondi accretion ignores

the possibility that gas particles may have angular momentum. The gas in the simulation used in Hopkins et al. (2016) is primarily cold and is supported by angular momentum rather than radiation pressure. Observations show that especially in gas-rich galaxies that naturally host molecular torii, the r<100 pc cold gas reservoir is large, has significant angular momentum, and is the primary candidate for black hole accretion fueling (Davies et al. 2004; Hicks et al. 2013; Medling et al. 2014; Lin et al. 2016; Gaspari et al. 2015). Ignoring the angular momentum of the cold gas is likely the primary cause of the overestimate that Bondi accretion makes both in Hopkins et al. (2016) the aperture sizes of r$\lesssim$327 pc in this work.

The performance of Bondi accretion between 200-500 pc is more realistic, and it even dips below the X-ray derived accretion rates for very large (r$\geq$398) apertures. This is because, as is apparent in Figure 2, the cold gas has much lower average densities at large distances from the SMBH.

If NGC 1068 is typical, these results suggest that the usage of pure Bondi accretion is likely to struggle to accurately predict black hole accretion rates. From our example, the accuracy of Bondi predictions depends heavily on the size of the black hole kernel used to calculate nuclear conditions, overpredicting in the small radius limit and underpredicting in the large radius limit. Understanding the physical mechanisms that drive accretion on the sub-grid scales in galactic nuclei can inform the future development of accretion prescriptions. The Bondi prescription applies free-fall to particles inside the Bondi radius, but our results suggest that angular momentum plays an important role in some nuclei.

6. CONCLUSIONS AND FUTURE EXPANSION OF THIS PROJECT

In this study we estimate a Bondi accretion rate as a function of radius for NGC 1068 using two different molecular gas tracers, and compare the result to the direct accretion rate derived from hard X-ray luminosity of the AGN. Compared to warm H_2 gas, CO gas is the dominant mass carrier close to the SMBH. Following this, the cold gas derived Bondi accretion rate estimate outpaces the X-ray derived value by more than 1 order of magnitude at aperture sizes r$\lesssim$125 pc and up to 4 dex inside the smallest apertures. In the case of warm gas Bondi accretion where the enclosed mass involved in the calculation is negligible, and in the cold gas case in aperture sizes of r$\gtrsim$327 pc, the Bondi accretion rate is instead lower than or equal to the X-ray accretion rates.

This paper is a pilot for a wider study of AGN and accretion prescriptions. Direct probes of sub-grid accretion prescriptions may, as our sample expands, help identify which physical processes dominate accretion on a variety of spatial scales, and in turn provide recommendations for appropriate sub-grid prescriptions to describe them. The results in this work support previous evidence that in high resolution cosmological simulations, applying a Bondi accretion prescription can lead to large overestimates of $\dot{M}_{BH}$ and therefore large overestimates of AGN feedback, which in turn impacts the global galaxy evolutionary track. We note that this is a test for a specific Seyfert 2 AGN. To make more robust recommendations about the application of the Bondi accretion prescription for sub-grid accretion physics we must directly test Bondi on more galaxies.

REFERENCES

Anglés-Alcázar, D., Davé, R., Faucher-Giguère, C.-A., Özel, F., & Hopkins, P. F. 2017, MNRAS, 464, 2840

Antonucci, R. 1993, ARA&A, 31, 473

Astropy Collaboration et al. 2013, A&A, 558, A33

—. 2018, AJ, 156, 123

—. 2022, ApJ, 935, 167

Barnouin, T., Marin, F., Lopez-Rodriguez, E., Huber, L., & Kishimoto, M. 2023, A&A, 678, A143

Barthelmy, S. D., et al. 2005, SSRv, 120, 143

Behroozi, P. S., Wechsler, R. H., & Conroy, C. 2013, ApJ, 770, 57

Bocquet, S., Saro, A., Dolag, K., & Mohr, J. J. 2016, MNRAS, 456, 2361

Bolatto, A. D., Wolfire, M., & Leroy, A. K. 2013, ARA&A, 51, 207

Bondi, H. 1952, MNRAS, 112, 195

Bondi, H., & Hoyle, F. 1944, MNRAS, 104, 273

Booth, C. M., & Schaye, J. 2009, MNRAS, 398, 53

Briggs, D. S. 1995, in American Astronomical Society Meeting Abstracts, Vol. 187, American Astronomical Society Meeting Abstracts, 112.02

Burns, J. O., Feigelson, E. D., & Schreier, E. J. 1983, ApJ, 273, 128

Cardelli, J. A., Clayton, G. C., & Mathis, J. S. 1989, ApJ, 345, 245

Cielo, S., Bieri, R., Volonteri, M., Wagner, A. Y., & Dubois, Y. 2018, MNRAS, 477, 1336

Comrie, A., et al. 2021, CARTA: The Cube Analysis and Rendering Tool for Astronomy

Curtis, H. D. 1918, Publications of Lick Observatory, 13, 9

Davé, R., Anglés-Alcázar, D., Narayanan, D., Li, Q., Rafieferantsoa, M. H., & Appleby, S. 2019a, MNRAS, 486, 2827

—. 2019b, MNRAS, 486, 2827

Davies, R., Ward, M., & Sugai, H. 2000, ApJ, 535, 735

Davies, R. I., Sternberg, A., Lehnert, M., & Tacconi-Garman, L. E. 2003, ApJ, 597, 907

Davies, R. I., Sternberg, A., Lehnert, M. D., & Tacconi-Garman, L. E. 2005, ApJ, 633, 105

Davies, R. I., Tacconi, L. J., & Genzel, R. 2004, ApJ, 613, 781

Di Matteo, T., Quataert, E., Allen, S. W., Narayan, R., & Fabian, A. C. 2000, MNRAS, 311, 507

Di Matteo, T., Springel, V., & Hernquist, L. 2005, Nature, 433, 604

16

Dolag, K., Komatsu, E., & Sunyaev, R. 2016, MNRAS, 463, 1797

Dubois, Y., Gavazzi, R., Peirani, S., & Silk, J. 2013a, MNRAS, 433, 3297

Dubois, Y., Peirani, S., Pichon, C., Devriendt, J., Gavazzi, R., Welker, C., & Volonteri, M. 2016, MNRAS, 463, 3948

Dubois, Y., Pichon, C., Devriendt, J., Silk, J., Haehnelt, M., Kimm, T., & Slyz, A. 2013b, MNRAS, 428, 2885

Fabian, A. C. 2012, ARA&A, 50, 455

Ferrarese, L., & Merritt, D. 2000, ApJL, 539, L9

Feruglio, C., Maiolino, R., Piconcelli, E., Menci, N., Aussel, H., Lamastra, A., & Fiore, F. 2010, A&A, 518, L155

Gallimore, J. F., Baum, S. A., O'Dea, C. P., & Pedlar, A. 1996, ApJ, 458, 136

Gallimore, J. F., & Impellizzeri, C. M. V. 2023, ApJ, 951, 109

Gallimore, J. F., et al. 2016, ApJL, 829, L7

Gámez Rosas, V., et al. 2022, Nature, 602, 403

García-Burillo, S., et al. 2014, A&A, 567, A125

—. 2019, A&A, 632, A61

Gaspari, M., Brighenti, F., & Temi, P. 2015, A&A, 579, A62

Gebhardt, K., et al. 2000, ApJL, 539, L13

Gehrels, N., et al. 2004, ApJ, 611, 1005

Genel, S., et al. 2014, MNRAS, 445, 175

Goldsmith, P. F., & Langer, W. D. 1999, ApJ, 517, 209

Greenhill, L. J., & Gwinn, C. R. 1997, Ap&SS, 248, 261

Greenhill, L. J., Gwinn, C. R., Antonucci, R., & Barvainis, R. 1996, ApJL, 472, L21

Gupta, K. K., et al. 2024, A&A, 691, A203

Hagiwara, Y., Baan, W. A., Imanishi, M., & Diamond, P. 2024, MNRAS, 528, 3668

Harris, C. R., et al. 2020, Nature, 585, 357

Hicks, E. K. S., Davies, R. I., Maciejewski, W., Emsellem, E., Malkan, M. A., Dumas, G., Müller-Sánchez, F., & Rivers, A. 2013, ApJ, 768, 107

Hinshaw, G., et al. 2009, ApJS, 180, 225

Hirschmann, M., Dolag, K., Saro, A., Bachmann, L., Borgani, S., & Burkert, A. 2014, MNRAS, 442, 2304

Hobbs, A., Power, C., Nayakshin, S., & King, A. R. 2012, MNRAS, 421, 3443

Holden, L. R., & Tadhunter, C. N. 2023, MNRAS, 524, 886

Hopkins, P. F., & Quataert, E. 2011, MNRAS, 415, 1027

Hopkins, P. F., Torrey, P., Faucher-Giguère, C.-A., Quataert, E., & Murray, N. 2016, MNRAS, 458, 816

Howarth, I. D. 1983, MNRAS, 203, 301

Hoyle, F., & Lyttleton, R. A. 1939, Proceedings of the Cambridge Philosophical Society, 35, 405

Hunter, J. D. 2007, Computing in Science & Engineering, 9, 90

Hviding, R. E., Hickox, R. C., Väisänen, P., Ramphul, R., & Hainline, K. N. 2023, AJ, 166, 111

Imanishi, M., Nakanishi, K., Izumi, T., & Wada, K. 2018, ApJL, 853, L25

Imanishi, M., et al. 2020, ApJ, 902, 99

Jaffe, W., et al. 2004, Nature, 429, 47

Khandai, N., Di Matteo, T., Croft, R., Wilkins, S., Feng, Y., Tucker, E., DeGraf, C., & Liu, M.-S. 2015, MNRAS, 450, 1349

Kormendy, J., & Ho, L. C. 2013, ARA&A, 51, 511

Krimm, H. A., et al. 2013, ApJS, 209, 14

Kumar, P. 1999, ApJ, 519, 599

Larkin, J., et al. 2006, in Society of Photo-Optical Instrumentation Engineers (SPIE) Conference Series, Vol. 6269, Ground-based and Airborne Instrumentation for Astronomy, ed. I. S. McLean & M. Iye, 62691A

Lin, M.-Y., et al. 2016, MNRAS, 458, 1375

Lockhart, K. E., et al. 2019, AJ, 157, 75

Lodato, G., & Bertin, G. 2003, A&A, 398, 517

Lyke, J., et al. 2017, OSIRIS Toolbox: OH-Suppressing InfraRed Imaging Spectrograph pipeline, Astrophysics Source Code Library, record ascl:1710.021

Magorrian, J., et al. 1998, AJ, 115, 2285

Markevitch, M. 1998, ApJ, 504, 27

Martins, L. P., Rodríguez-Ardila, A., de Souza, R., & Gruenwald, R. 2010, MNRAS, 406, 2168

Matt, G., et al. 1997, A&A, 325, L13

May, D., & Steiner, J. E. 2017, MNRAS, 469, 994

McConnell, N. J., & Ma, C.-P. 2013, ApJ, 764, 184

Medling, A. M., et al. 2014, ApJ, 784, 70

Meenakshi, M., et al. 2022, MNRAS, 516, 766

Morganti, R. 2017, Frontiers in Astronomy and Space Sciences, 4, 42

Müller Sánchez, F., Davies, R. I., Eisenhauer, F., Tacconi, L. J., Genzel, R., & Sternberg, A. 2006, A&A, 454, 481

Müller-Sánchez, F., Prieto, M. A., Hicks, E. K. S., Vives-Arias, H., Davies, R. I., Malkan, M., Tacconi, L. J., & Genzel, R. 2011, ApJ, 739, 69

Mushotzky, R. F. 1984, Physica Scripta Volume T, 7, 157

Mutie, I. M., et al. 2024, MNRAS, 527, 11756

Netzer, H., & Trakhtenbrot, B. 2014, MNRAS, 438, 672

Ott, T. 2012, QFitsView: FITS file viewer, Astrophysics Source Code Library, record ascl:1210.019

Pillepich, A., et al. 2018a, MNRAS, 473, 4077

—. 2018b, MNRAS, 473, 4077

Raban, D., Jaffe, W., Röttgering, H., Meisenheimer, K., & Tristram, K. R. W. 2009, MNRAS, 394, 1325

Ricci, C., et al. 2017, ApJS, 233, 17

Rosas-Guevara, Y. M., et al. 2015, MNRAS, 454, 1038

Saito, T., et al. 2022, ApJ, 935, 155

Schaye, J., et al. 2015, MNRAS, 446, 521

Springel, V., Di Matteo, T., & Hernquist, L. 2005, MNRAS, 361, 776

Springel, V., & Hernquist, L. 2005, ApJL, 622, L9

Storchi-Bergmann, T., McGregor, P. J., Riffel, R. A., Simões Lopes, R., Beck, T., & Dopita, M. 2009, MNRAS, 394, 1148

Taylor, P., & Kobayashi, C. 2015, MNRAS, 448, 1835

Torrey, P., Vogelsberger, M., Genel, S., Sijacki, D., Springel, V., & Hernquist, L. 2014, MNRAS, 438, 1985

Tremmel, M., Karcher, M., Governato, F., Volonteri, M., Quinn, T. R., Pontzen, A., Anderson, L., & Bellovary, J. 2017, MNRAS, 470, 1121

Tristram, K. R. W., Burtscher, L., Jaffe, W., Meisenheimer, K., Hönig, S. F., Kishimoto, M., Schartmann, M., & Weigelt, G. 2014, A&A, 563, A82

Valentini, M., et al. 2020, MNRAS, 491, 2779

Veilleux, S., Goodrich, R. W., & Hill, G. J. 1997, ApJ, 477, 631

Viti, S., et al. 2014, A&A, 570, A28

Vogelsberger, M., Genel, S., Sijacki, D., Torrey, P., Springel, V., & Hernquist, L. 2013, MNRAS, 436, 3031

Vogelsberger, M., et al. 2014, MNRAS, 444, 1518

Vollmer, B., Schartmann, M., Burtscher, L., Marin, F., Hönig, S., Davies, R., & Goosmann, R. 2018, A&A, 615, A164

Vollmer, B., et al. 2022, A&A, 665, A102

Wada, K., Kudoh, Y., & Nagao, T. 2023, MNRAS, 526, 2717

Wakelam, V., et al. 2017, Molecular Astrophysics, 9, 1

Weinberger, R., et al. 2017, MNRAS, 465, 3291

Wetzel, A., et al. 2023, ApJS, 265, 44

Williamson, D., Hönig, S., & Venanzi, M. 2020, ApJ, 897, 26

Wilson, A. S., & Ulvestad, J. S. 1983, ApJ, 275, 8

Wilson, T. L., Rohlfs, K., & Hüttemeister, S. 2013, Tools of Radio Astronomy

Wright, E. L. 2006, PASP, 118, 1711